Journal of Materials Chemistry A

Accepted Manuscript

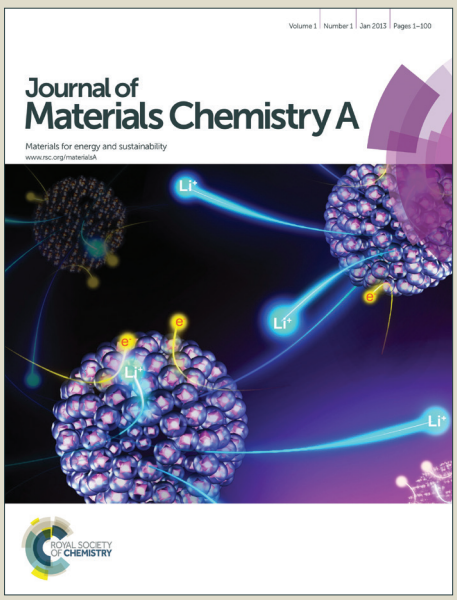

ROYAL SOCIETY OF CHEMISTRY

www.rsc.org/materialsA

Unique Synthesis of Mesoporous Peapod-like $NiCo_2O_4$-C Nanorods Array as Enhanced Anode for Lithium Ion Batteries

Liang Peng, Huijiuan Zhang, Yuanjuan Bai, Jiao Yang, Yu Wang*

The State Key Laboratory of Mechanical Transmissions and School of Chemistry and Chemical Engineering, Chongqing University, Chongqing 400044, China

E-mail: wangy@cqu.edu.cn; prospectwy@gmail.com

Keywords: mesoporous, $NiCo_2O_4$, carbon, capacity, lithium ion batteries

Abstract

Herein, a novel peapod-like $NiCo_2O_4$-C nanorods array on 3D Ni-foam is synthesized for the first time and use as anode for lithium ion batteries. The nanorods array grows directly on 3D Ni-foam by a facile route, including hydrothermal reaction and subsequent annealing at a setting temperature. Different from the previous reports, the as-prepared peapod-like $NiCo_2O_4$-C composite in our experiments exhibit both mesoporosity and excellent conductivity, and meanwhile, the stable core-shell structure provide an express purposes for improving electren transfer and electrolyte penetration when applied in lithium ion batteries. When tested in the electrochemical system, the as-prepared samples demonstrate excellent electrochemical performances, such as enhanced rate capability (a reversible capability of 664 mAh g^{-1} at 2000 mA g^{-1}) as well as a high coulombic efficiency (of coulombic efficiency of 97% can be obtained after 200 cycles at 100 mA g^{-1}).

Introduction

Because the growing concerns consist of increased oil prices, environmental issues and the stretched energy situation, various energy storage systems have been designed and presented, especially electrochemical energy storage devices, which have been

extensively studied and identified as promising green energy storage systems.[1, 2] Lithium ion batteries (LIBs), especially with high rate, long lifespan and high energy density properties, are considered as the most important energy storage and conversion device, such as portable electric devices and electric vehicles.[3]

LIBs consist of four parts: cathode electrode, anode electrode, separator and electrolyte.[4, 5] Recently, various active materials have been studied for LIBs as anode or cathode materials including metal (Sn),[6] metal oxides (CuO, Fe_2O_3, SnO_2, $NiCo_2O_4$, etc.),[7-9] metal sulfides (CoS, MoS_2, etc.),[10, 11] carbon materials (graphene, carbon nanotube, etc.),[12, 13] conducting polymers (polypyrrole, polyaniline, polythiophene, etc.),[14, 15] silicon,[16] sulphur,[17, 18] and so on. Among all these above mentioned active materials, transition metal oxides have important properties of semiconductors with extensive applications in energy storage due to their unique electrochemical performances. However, acting as an alternative promising anodic material for LIBs, the properties of $NiCo_2O_4$ have been studied less.[19, 20] As a LIBs anode material, $NiCo_2O_4$ can react with eight Li-ion per formula unit with a high theoretical capacity of ~890 mAh g^{-1}. Meanwhile, as a binary metal oxide, $NiCo_2O_4$ has much better electrical conductivity and electrochemical performances than single cobalt oxides or nickel oxides.[19, 21] The higher electrical conductivity which is favorable for the fast electrons transfer in an electrode, enable to obtain much higher specific capacity and better cycling performance. Besides the above mentioned advantages, other features, such as abundant resources, low-cost, environmental friendliness, and coming from both cobalt and nickel ions, also imply its promising electrochemical capacitors (ECs) application as an alternative Li-ion batteries anode electrode.

However, large volume changes appear during Li-ion charge-discharge process due to the conversion reaction mechanism, which lead to the pulverization of electrode materials and detachment from the current collector, thereby resulting in poor cycling performance.[22-24] In attempt to solve this problem, it is an efficient way to design porous nanostructures with highly accessible surfaces and unique sizes and morphology.[25, 26] With the merit of mesopores, electrodes materials could exhibit superior electrochemical performances because of their high specific surface areas

which is in favor for the interface contact between electrode and electrolyte, and meanwhile, allow the electrolyte to permeate into the electrode materials easy, leading to a great flux of Li-ion across the interface and providing effective space for volume expansion during the charge-discharge cycle. The other effective strategy to solve the above problem is to prepare nanostructured materials with coating conducting thin layers, including origin poly-layer, carbon layer, metal layers, and so on.[27-29] Due to the protection by the coating-layers, the $NiCo_2O_4$ anode material can relieves the stress induced by volume expansion or contraction, and then obtain improved capacity retention. In addition, the introduction of coating-layers also can increase the electronic conductivity, and avoid the aggregation and pulverization of the $NiCo_2O_4$ anode material during Li-ion insertion-extraction process.

In the present work, we introduce a facile approach to prepare a unique peapod-like architectural array with $NiCo_2O_4$ nanoparticles encapsulated in carbon nanorods and directly grow on the 3D Ni-foam. The unique peapod-like nanocomposite array has various admirable characters including small size of the peapods, good graphitization of carbon fibers, remarkable mesoparous property and stable nanostructure. All these advantages sufficiently verify excellent performances in LIBs electrochemical measurement, such as high charge-discharge capacities, excellent rate capabilities, and exemplary cycling performances. It is believed that this novel nanocomposite has great practical application in both the energy and power storage of Li-ion batteries.

Experimental Section

Synthesis of Ni-Co precursor nanorods array on the Ni-foam

All materials or chemicals were used as received and analytical grade. In a typical experiment,[30, 31] Ni-Co precursor nanorods array was synthesized on Ni-foam by a simple hydrothermal method. The experimental details are as follows: 10 mL $Ni(NO_3)_2 \cdot 6H_2O$ (0.2 mol L^{-1}), 10 mL $Co(NO_3)_2 \cdot 6H_2O$ (0.4 mol L^{-1}), 10 mmol NH_4F, and 15 mmol urea were dissolved in 20 mL Deionized water (DI-water) and stirred to form a pink solution. The Ni-foam (1.0 cm × 3.0 cm) was careful cleaned with concentrated HCl solution with ultrasonic treatment for 10 min, and then further

cleaned by DI-water and absolute ethanol to ensure the surface of the Ni-foam was well cleaned. The above aqueous reagent solution and the Ni-foam substrate were then placed in a 50 mL Teflon-lined stainless-steel autoclave. The autoclave was sealed and maintained at 120 ^{o}C for 9 h, and then cooled down to room temperature. The array procures was collected and rinsed use DI-water and absolute ethanol several times, followed by dried at 60 ^{o}C in a vacuum drying oven for 12h to obtain the precursors (Ni-Co precursors).

Synthesis of the peapod-like NCO-C nanorods array on Ni-foam

The Ni-Co precursors on Ni-foam (1.0 cm × 3.0 cm) was ultrasonically mixed with 5 mL glucose aqueous solution (1 mol g^{-1}) and 35 mL DI-water for 10 min, then transferred into a 50 mL Teflon-lined autoclave.[32, 33] The autoclave was sealed and maintained at 180 ^{o}C for 6 h, and then cooled down to room temperature. After that, the samples were collected and ringed with DI-water and absolute ethanol several times. The Ni-Co precursors were coated with polymerized glucose molecules on the surface. Then, the coating precursors was annealed at 700 ^{o}C for 200 min in a H_2 atmosphere and thereby annealed at 250 ^{o}C for 100 min with a ramping rate of 2 ^{o}C min^{-1} to form the peapod-like structure composite where the $NiCo_2O_4$ nanoparticales encapsulated in carbon nanorods on the 3D Ni-foam.[34]

Carbon content tests

In order to precisely calculate the performances of the LIBs, we also fabricated the peapod-like NCO-C nanorods array on a flat Ni-sheet and then scraped off the nanocomposite use a thin knife. After that, the NCO-C samples (200 mg) were uniformly mixed with concentrated HCl solution for 2 days to completely dissolve the $NiCo_2O_4$ nanoparticales. The remaining carbon was carefully collected, rinsed and dried in a vacuum drying oven at 60 ^{o}C for overnight. The carbon content in the NCO-C samples was calculated using this formula:

$$C\% = [W(C)/W(NCO\text{-}C)] \times 100\%$$

Where W(C) and W(NCO-C) are the weights of the remaining carbon and primary

peapod-like samples, respectively. Using this method, the concentration of carbon in the nanocomposite is about 5.9 wt%, which is very low contribution to the capacity during electrochemical tests.

Material Characterizations.

The fabricated materials were characterized by powder X-ray diffraction (Bruker D8 Advance X-ray diffractometer) with Cu Kα radiation, scanning electron microscope (SEM, JEOL, JSM-7800F) with an energy dispersive spectrometer (EDS), transmission electron microscopy (TEM, JEOL, JEM-2100F), Brunauer-Emmett-Teller surface-area and pore-size analyzer (BET, Quantachrome Autosorb-6B),Raman spectroscopy (RENISHAW Invia Raman Microscope, voltage (AC) 100-240 V, power 150 W) and X-ray photoelectron spectroscopy (XPS, ESCALAB 250Xi).

Electrochemical Measurements

Electrochemical measurements were performed with R2032 coin-type cells. A Ni-foam loaded with NCO-C nanosheets array was cut into smaller pieces (1 cm × 1 cm) and used as binder-free working electrodes directly. A lithium metal was used as the counter and reference electrode and a Celgard 2400 membrane was used as the cell separator. The electrolyte was 1 M $LiPF_6$ in ethylene carbonate and diethyl carbonate (EC-DEC, v/v=1:1). The cells were constructed in an Ar-filled glove box. The galvanostatic cycling was performed on Neware battery testing system, and cyclic voltammetry (CV) was collected using Autolab (model of AUT71740). The electrochemical impedance measurements were carried out by applying an AC voltage of 5 mV in the frequency from 0.01 Hz to 100 kHz. The specific capacity and current density were calculated based on the mass of the active material in the working electrode. The electrochemical tests were carried out using a three electrode system.

Results and discussion

Structural and morphological characterization

In Fig. 1, the fabrication route and the final unique electrode architectures developed in this study are schematically displayed. Firstly, as the typical synthesis

process, the Ni-Co polymerized nanorods precursor (Ni-Co Precursors) is grow vertically on 3D Ni-foam by a hydrothermal reaction.[31, 35] Secondly, a thin layer of carbonized glucose molecule on the Ni-Co Precursors surface *via* a hydrothermal treatment using glucose as green carbon source. Thirdly, the carbonized glucose coating precursors are annealed in CVD and Muffle-Furnace oven at the corresponding elevated temperatures in Ar and air atmospheres, respectively, resulting in the final peapod-like samples (NCO-C).

Scanning electron microscopy (SEM) is employed to investigate the micro-morphologies and structures of the Ni-Co Precursors. As shown in Fig. 2a, it shows that the nanorods precursor is fully and uniformly grown on the Ni-foam with high density. In the locally magnified SEM image, as shown in Fig. 2b, some nanorods with a uniform diameter of about ~10-30 nm could be apparently found. If it was carefully observed, we can easily discover that these nanorods directly grow on the Ni-foam and along the same direction with a certain distance interval, which is favorable for the subsequent glucose molecule coating. The film cross-sectional image in Fig. 2c indicates the nanorods precursor grows vertical on the Ni-foam substrate and the length of these nanorods are about ~ 2.5 um. From Fig. 2d, good and tightening contact between the Ni-Co Precursors and Ni-foam can be clearly revealed. A wide X-ray diffraction angle of 2θ=20-70 ^{o} (XRD), as showed in Fig. S1, proves the coexistence of $Co_2(CO_3)(OH)_2 \cdot 0.11H_2O$ (JCPDS:48-0083) and $Ni_2(CO_3)(OH)_2 \cdot 4H_2O$ (JCPDS:38-0714) in the Ni-Co Precursors.

The more information about the surface electronic states of the as-prepared NCO-C can be further characterized by X-ray photoelectron spectroscopy (XPS) measurements and the corresponding results are presented in Fig.S2. The high-resolution spectrum for the O 1s region (Fig.S2a) indicates two oxygen contributions. Usually, the peak at 531.2 eV is associated with detects, contaminants, and a number of surface species such as hydroxyls, chemisorbed oxygen, under-coordinated lattice oxygen, or intrinsic species to the surface of the spinel. Specifically, the peak at 529.4 eV is typical of metal-oxygen bonds.[36] By using Gaussian fitting method, the Ni 2p emission spectrum (Fig.S2b) is best fitted by two

spin-orbit doublets, characteristic of Ni^{2+} and Ni^{3+}, and two shakeup satellite peaks (denoted as "sat."). [37, 38] Meanwhile, the Co 2p spectrum is also best fitted with considering two spin-orbit doublets, characteristic of Co^{2+} and Co^{3+}, and two couples of shakeup satellites (Fig.S2c). [39] The composition and phase purity of the NCO-C composite are characterized by XRD and the result reveals that all the reflection peaks can be indexed to cubic $NiCo_2O_4$ with a special spinel structure corresponding to the JCPDF card (No. 20-0781) (Fig. 3), and no additional peaks can be detected implying that the final samples have been fabricated without impurity. [40, 41] In addition, the NCO-C composite is scraped off the Ni-foam and further demonstrated by energy-dispersive X-ray spectroscopy (EDX) (Fig. S3), which reveals an atomic Ni/Co ratio of 1:2, wherein the elements Si is from the silicon wafer.

SEM and TEM are employed to investigate the so-collected samples as shown in Fig. 4. From Fig. 4a it can reveal that the NCO-C samples could be prepared in large scales using our synthetic method, and show 1-D nanostructures with a uniform morphology. By carefully observing, as shown in Fig. 4b, we can find that these 1-D nanostructures originated from the same starting point and grew along the common direction, which is almost perpendicular to the surface of Ni-foam. The corresponding magnified image shown in Fig. 4c reveals that the samples exhibit uniform nanorod-shaped morphology with a certain distance interval to each other. High-magnification SEM image (Fig. 4d) indicates that many peapod-like nanorods are aligned together, and interestingly, the encapsulated $NiCo_2O_4$ nanoparticles can be clearly observed with their distribution along the carbon rod. Another cross-section SEM image (shown in Fig. 4e) reveals that the length of the as-prepared NCO-C nanorods composite is around 2 μm. To further reveal the structural details about the NCO-C composite, TEM is used to collect more information as shown in Fig 4f-h. From Fig 4f and g, especially in Fig. 4g, it can be detected that all the samples possess peapod-like configuration, where isolated $NiCo_2O_4$ nanoparticles are separated from each other and uniformly distributed in corresponding carbon rod with regular interval distance of 10-30 nm. HRTEM image (Fig. 4h) for the ultimately products of NCO-C composite shows that the encapsulated well-crystallized $NiCo_2O_4$ nanoparticles are

coated with carbon layers to form the 1-D hierarchical structures. Distances of 0.47 and 0.28 nm correspond to their equivalent crystal planes of (111) and (220) for spinal $NiCo_2O_4$, respectively.[42, 43] From the image we can know that the ultimately synthesized NCO-C composite maintain the well-morphology of peapod-like nanorods array during the annealing in air.[32, 33] Furthermore, the corresponding TEM-EDS elemental mapping analysis of the NCO-C composite also confirms the NCO-C hierarchical nanostructure, as shown in Fig.S4, where contains the mappings for Ni, Co, O and C, showing good distribution of elements in the composite.

The specific surface area and porous distribution of the NCO-C composite are determined by nitrogen-adsorption/desorption analysis at 77K, which is shown in Fig. 5. As shown in Fig. 5a, a typical Langmuir type Ⅳ isotherm with an apparent hysteresis loop, which demonstrate the mesoporous nature of the as-prepared sample.[44] Meanwhile, from Fig. 5a we can see the composite exhibits a high Brunauer-Emmett-Teller (BET) specific surface area of 200.75 m^2 g^{-1}. The porous size distribution calculated from the adsorption isotherm using the BJH model (Fig. 5b), indicates that most pores size fall into the range of 2-5 nm, and the pores size centered at 3 nm.[45] In fact, the mesoporosity could be reasonably inferred from the release of CO, CO_2, H_2O and ammonia during the thermal decomposition of the Ni-Co precursor. Such a porous nanostructure could effectively promote electrode materials electrochemical performances, as it can greatly enhance the diffusion of electrolyte to electrode materials and buffer the large volume change in the anode during the fast charge-discharge cycles. Raman spectroscopy is to characterize the state of carbon in the peapod-like composite (shown in Fig. S5). Two main bands are observed at around 1590 and 1380 cm^{-1}, which is corresponding to designated as the G band and D band, respectively. The G band corresponds to graphite in-plane vibrations with E_{2g} symmetry, while the D band is attributed to disorder-allowed phonon modes. Usually, the ratio value I_D/I_G can be used to evaluate the degree of disorder for carbon layer structure. As the I_D/I_G ratio increases, the defect structure increases accordingly, meaning the degree of graphitization becomes low.[46, 47] The value of the I_D/I_G for the NCO-C composite is around ~1, which suggests that the

carbon have a relatively high degree of graphitization.

Electrochemical characteristics

The electrochemical performances measurements of the NCO-C composite are configured as CR2032 coin cells without using ancillary binders or conducting additives. Fig. 6a shows the cyclic voltammetry (CV) curves of the electrodes at a scanning rate of 0.5 mV s^{-1} in the voltage of 0.01-3.0 V (vs Li/Li^+). Usually, the voltammogram for the first cycle is different from that of others. In the first cathodic scan, the intense peak at 0.86 V can be considered as the reduction of Co^{3+} and Ni^{2+} to corresponding metallic Co and Ni. In the subsequent cycles, the main reduction peaks shift to higher potential at 0.92 V. Meanwhile, the following anodic sweep is characterized by two oxidation peaks at ~1.6 V and 2.2 V, which can be attributed to the oxidation of Ni to Ni^{2+} and Co to Co^{3+}, respectively. On the basis of the cyclic voltammograms (CV), and together with the previous reports, the electrochemical cycles involved during the Li-ion insertion-extraction process can be classified as follow:[22, 48]

$$NiCo_2O_4 + 8\ Li^+ + 8\ e^- \rightarrow Ni + 2Co + 4Li_2O \quad (1)$$

$$Ni + Li_2O \leftrightarrow NiO + 2Li^+ + 2e^- \quad (2)$$

$$Co + Li2O \leftrightarrow CoO + 2Li^+ + 2e^- \quad (3)$$

$$CoO + 1/3Li_2O \leftrightarrow 1/3Co_3O_4 + 2/3Li^+ + 2/3e^- \quad (4)$$

The charge-discharge tests of the NCO-C anode electrode in the voltage window of 0.01-3.0 V (vs. Li/Li^+) at 100 mA $g^{-1}$are shown in Fig. 6b. The first discharge capacity is 1682 mAh g^{-1} which is much higher than the theoretically capacity (890 mAh g^{-1}) greatly due to the formation of solid electrolyte interface (SEI) film and as well as forming a organic polymeric/gel-like layer by electrolyte decomposition.[49] In subsequent charge-discharge processes, the cycle profiles tend to be stable and indicate nearly same electrochemical performances with approximate charge and discharge capacities of 1081 and 1152 mAh g^{-1}. Interestingly, these capacities are unexpectedly higher than the theoretically capacity, which is possible due to two

reasons: (1) the reversible formation-dissolution of the polymer/gel-like film; (2) porous of the outside carbon fiber and inside active materials can provide some effective sites for Li^+ insertion-extraction.

To better understand the electrochemical behavior of the NCO-C composite, we also studied its rate capability as shown in Fig. 7a. The as-prepared NCO-C anode electrode is evaluated at various current densities (100 to 2000 mA g^{-1}). The discharge capacity can reach 1150 mAh g^{-1} at a low rate current of 100 mA g^{-1} after 10 cycles. When the current densities increased stepwise to 300, 500, 1000 and 2000 mA g^{-1}, the results show good rate capability with average discharge capacity of 984, 918, 764 and 653mAh g^{-1}, respectively. Upon altering the current density back to 300 and 100 mA g^{-1}, the discharge capacities of 963 and 1024 mAh g^{-1} can be received. Fig. 7b presents the capacity retention and Coulombic efficiency of the NCO-C composite. After 200 cycles, the NCO-C composite electrode still exhibits a stable discharge capacity of 1183 mAh g^{-1} (about 97% of the second discharge capacity), which is most because the unique core-shell structure can effectively alleviate the pulverization problem.

The cyclic performance of the NCO-C composite at the currents of 500 and 2000 mA g^{-1} are further demonstrated in Fig. 7c. The first capacities of the NCO-C composite are 1081 and 884 mAh g^{-1} at the current densities of 500 and 2000 mA g^{-1}, respectively, and interesting to reveal that there is a trend of the gradual stable capacities after 10 and 50 cycles at the rate of 500 and 2000 mA g^{-1}. After 200 cycles, the discharge capacities are retained at 863 and 594 mAh g^{-1} at the current densities of 500 and 2000 mA g^{-1}, respectively, which are almost 96% and 67% of the theoretically capacities. As shown in Fig. S6, the randomly dispersed Peapod-like NCO-C composites, which are scraped off from the Ni-foam, were tested at a current density of 500 mAh g^{-1}. With the development of galvanostatic measurement, the specific capacity finally retains at 849 mAh g^{-1} after 200 cycles**,** which partly lower than that of the peapod-like composite directly grown on Ni-fom (863 mAh g^{-1}). We also compared the current work with other $NiCo_2O_4$-based high rate electrode materials reported in the recent study work, such as hierarchical $NiCo_2O_4$ nanowire

arrays,[50] porous $NiCo_2O_4$ nanoplates,[51] mesoporous $NiCo_2O_4$ nanosheets,[40, 52] flower-like $NiCo_2O_4$,[22] $NiCo_2O_4$ nanoparticles embedded in 3DHPC,[41] $NiCo_2O_4$ mesoporous microsphere,[53] hollow $NiCo_2O_4$ nanocube,[54] quasi-single-crystalline $NiCo_2O_4$ nanoribbons,[55] and so on,[56] and these results are shown in Fig. 8. By comparison, these peapod-like NCO-C nanorods array composite indicates comparable electrochemical performance at various rate densities to commonly electrodes.

Conclusion

In summary, we have successfully developed a novel route toward NCO-C nanorods array grown directly on 3D Ni-form substrate, and form a binder free electrode for LIBs. The unique hierarchical nanostructure of the NCO-C composite combines the fascinating characters, including nano-size $NiCo_2O_4$ particles, large specific surface area, good conductivity and good structure stability of the nanorod arrays. Owing to the above mentioned advantages, the NCO-C composite exhibits excellent electrochemical performances, such as excellent rate capability (a reversible capability of 664 mAh g^{-1} at 2000 mA g^{-1}) as well as a high Coulombic efficiency (about Coulombic efficiency of 97% can be obtained after 200 cycles at 100 mA g^{-1}).

Acknowledgements

This work was financially supported by the Thousand Young Talents Program of the Chinese Central Government (Grant No.0220002102003), National Natural Science Foundation of China (NSFC, Grant No. 21373280,21403019), Beijing National Laboratory for Molecular Sciences (BNLMS) and Hundred Talents Program at Chongqing University (Grant No. 0903005203205).

Supporting Information Available: More EDS, Raman, XPS, TEM-Mapping dates are available in the supporting information for this paper.

Reference

1. N. Oyama, T. Tatsuma, T. Sato and T. Sotomura, *Nature*, 1995, **373**, 598-600.
2. W. Li, J. R. Dahn and D. S. Wainwright, *Science*, 1994, **264**, 1115-1118.
3. K. S. Kang, Y. S. Meng, J. Breger, C. P. Grey and G. Ceder, *Science*, 2006, **311**, 977-980.
4. M. J. Zou, M. Yashio, S. Gopukumar and J. I. Yamaki, *Chem. Mater.*, 2005, **17**, 1284-1286.
5. P. Balaya, *Energy Environ. Sci.*, 2008, **1**, 645-654.
6. N. Zhang, Q. Zhao, X. P. Han, J. G. Yang and J. Chen, *Nanoscale*, 2014, **6**, 2827-2832.
7. P. C. Lian, S. Z. Liang, X. F. Zhu, W. S. Yang and H. H. Wang, *Electrochim. Acta*, 2011, **58**, 81-88.
8. Y. M. Sun, X. L. Hu, W. Luo and Y. H. Huang, *J. Phys. Chem. C*, 2012, **116**, 20794-20799.
9. J. S. Xu and Y. J. Zhu, *ACS Appl. Mater. Interfaces*, 2012, **4**, 4752-4757.
10. X. P. Fang, C. X. Hua, X. W. Guo, Y. S. Hu, Z. X. Wang, X. P. Gao, F. Wu, J. Z. Wang and L. Q. Chen, *Electrochim. Acta*, 2012, **81**, 155-160.
11. W. W. Chen, T. T. Li, Q. Hu, C. P. Li and H. Guo, *J. Power Sources*, 2015, **286**, 159-165.
12. Z. L. Wang, D. Xu, H. G. Wang, Z. Wu and X. B. Zhang, *ACS Nano*, 2013, **7**, 2422-2430.
13. F. Liu, S. Y. Song, D. F. Xue and H. J. Zhang, *Adv. Mater.*, 2012, **24**, 1089-1094.
14. F. Wu, J. Z. Chen, L. Li, T. Zhao, Z. Liu and R. J. Chen, *ChemSuSChem*, 2013, **6**, 1438-1444.
15. L. Yang, V. A. Mihali, D. Brandell, M. Stromme and M. Sjodin, *J. Phys. Chem. C*, 2014, **118**, 25956-25963.
16. H. Yoo, J. I. Lee, H. Kim, J. P. Lee, J. Cho and S. Park, *Nano Lett.*, 2011, **11**, 4324-4328.
17. S. Xin, L. Gu, N. H. Zhao, Y. X. Yin, L. J. Zhou, Y. G. Guo and L. J. Wan, *J. Am. Chem. Soc.*, 2012, **134**, 18510-18513.
18. Y. S. Su, Y. Z. Fu and A. Manthiram, *Phys. Chem. Chem. Phys.*, 2012, **14**, 14495-14499.
19. X. Xu, B. Dong, S. Ding, C. Xiao and D. Yu, *J. Mater. Chem. A*, 2014, **2**, 13069-13074.
20. L. Shen, L. Yu, X. Y. Yu, X. Zhang and X. W. Lou, *Angew. Chem. Int. Ed.* , 2015, **54**, 1868-1872.
21. A. K. Mondal, D. Su, S. Chen, X. Xie and G. Wang, *ACS Appl. Mater. Interfaces*, 2014, **6**, 14827-14835.
22. L. Li, Y. Cheah, Y. Ko, P. Teh, G. Wee, C. Wong, S. Peng and M. Srinivasan, *J. Mater. Chem. A*, 2013, **1**, 10935-10945.

23. Y. G. Li, B. Tan and Y. Y. Wu, *Nano Lett.*, 2008, **8**, 265-270.

24. X. Y. Chen, H. L. Zhu, Y. C. Chen, Y. Y. Shang, A. Y. Cao, L. B. Hu and G. W. Rubloff, *ACS Nano*, 2012, **6**, 7948-7955.

25. S. Xiong, J. S. Chen, X. W. Lou and H. C. Zeng, *Adv. Funct. Mater.*, 2012, **22**, 861-871.

26. Y. Wang, H. Xia, L. Lu and J. Y. Lin, *ACS Nano*, 2010, **4**, 1425-1432.

27. W. H. Shi, J. X. Zhu, X. H. Rui, X. H. Cao, C. Chen, H. Zhang, H. H. Hng and Q. Y. Yan, *ACS Appl. Mater. Interfaces*, 2012, **4**, 2999-3006.

28. A. Trifonova, M. Winter and J. O. Besenhard, *J. Power Sources*, 2007, **174**, 800-804.

29. S. T. Myung, K. Izumi, S. Komaba, H. Yashiro, H. J. Bang, Y. K. Sun and N. Kumagai, *J. Phys. Chem. C*, 2007, **111**, 4061-4067.

30. G. Q. Zhang, H. B. Wu, H. E. Hoster, M. B. Chan-Park and X. W. Lou, *Energy Environ. Sci.*, 2012, **5**, 9453-9456.

31. D. Cai, B. Liu, D. Wang, L. Wang, Y. Liu, H. Li, Y. Wang, Q. Li and T. Wang, *J. Mater. Chem. A*, 2014, **2**, 4954-4960.

32. L. Peng, Y. Feng, Y. Bai, H.-J. Qiu and Y. Wang, *J. Mater. Chem. A*, 2015, **3**, 8825-8831.

33. Y. Wang, H. J. Zhang, L. Lu, L. P. Stubbs, C. C. Wong and J. Y. Lin, *ACS Nano*, 2010, **4**, 4753-4761.

34. H. J. Zhang, Y. J. Bai, Y. Zhang, X. Li, Y. Y. Feng, Q. Liu, K. Wu and Y. Wang, *Sci. Rep.*, 2013, **3**. 2717.

35. K. Xu, W. Li, Q. Liu, B. Li, X. Liu, L. An, Z. Chen, R. Zou and J. Hu, *J. Mater. Chem. A*, 2014, **2**, 4795-4802.

36. X.-F. Lu, D.-J. Wu, R.-Z. Li, Q. Li, S.-H. Ye, Y.-X. Tong and G.-R. Li, *J. Mater. Chem. A*, 2014, **2**, 4706-4713.

37. C. An, Y. Wang, Y. Huang, Y. Xu, C. Xu, L. Jiao and H. Yuan, *Crystengcomm*, 2014, **16**, 385-392.

38. H. Shi and G. Zhao, *J. Phys. Chem. C*, 2014, **118**, 25939-25946.

39. T. F. Hung, S. G. Mohamed, C. C. Shen, Y. Q. Tsai, W. S. Chang and R. S. Liu, *Nanoscale*, 2013, **5**, 12115-12119.

40. A. K. Mondal, D. W. Su, S. Q. Chen, K. Kretschmer, X. Q. Xie, H. J. Ahn and G. X. Wang, *ChemPhysChem*, 2015, **16**, 169-175.

41. L. Wang, L. Zhuo, C. Zhang and F. Zhao, *ACS Appl. Mater. Interfaces*, 2014, **6**, 10813-10820.

42. G. Y. Huang, S. M. Xu, Z. H. Xu, H. Y. Sun and L. Y. Li, *ACS. Appl. Mate.r Inter.*, 2014, **6**, 21325-21334.

43. T. Li, X. Li, Z. Wang, H. Guo and Y. Li, *J. Mater. Chem. A*, 2015, **3**, 11970-11975.

44. L. Shen, C. Yuan, H. Luo, X. Zhang, K. Xu and Y. Xia, *J. Mater. Chem.*, 2010, **20**, 6998-7004.

45. G.-N. Zhu, H.-J. Liu, J.-H. Zhuang, C.-X. Wang, Y.-G. Wang and Y.-Y. Xia, *Energy Environm. Sci.*, 2011, **4**, 4016-4022.

46. B. Li, C. Han, Y.-B. He, C. Yang, H. Du, Q.-H. Yang and F. Kang, *Energy Environ. Sci.*, 2012, **5**, 9595-9602.

47. L.-W. Zhang, H.-B. Fu and Y.-F. Zhu, *Adv. Funct. Mater.*, 2008, **18**, 2180-2189.

48. F. Zheng, D. Zhu and Q. Chen, *ACS Appl. Mater. Interfaces*, 2014, **6**, 9256-9264.

49. J. Y. Liao, X. Xiao, D. Higgins, G. Lui and Z. Chen, *ACS Appl. Mater. Interfaces*, 2014, **6**, 568-574.

50. G. Chen, J. yang, J. Tang and X. Zhou, *RSC Adv.*, 2015, **5**, 23067–23072.

51. Y. Chen, M. Zhuo, J. Deng, Z. Xu, Q. Li and T. Wang, *J. Mater. Chem. A*, 2014, **2**, 4449–4456.

52. Y. Chen, J. Zhu, B. Qu, B. Lu and Z. Xu, *Nano Energy*, 2014, **3**, 88-94.

53. J. Li, S. Xiong, Y. Liu, Z. Ju and Y. Qian, *ACS Appl. Mater. Interfaces*, 2013, **5**, 981-988.

54. H. Guo, L. Liu, T. Li, W. Chen, J. Liu and Y. Guo, *Nanoscale*, 2014, **6**, 5491-5497.

55. B. S. Li, J. K. Feng, Y. T. Qian and S. L. Xiong, *J. Mater. Chem. A*, 2015, **3**, 10336-10344.

56. T. Li, X. Li, Z. Wang, H. Guo and Y. Li, *J. Mater. Chem. A*, 2015, **3**, 11970–11975.

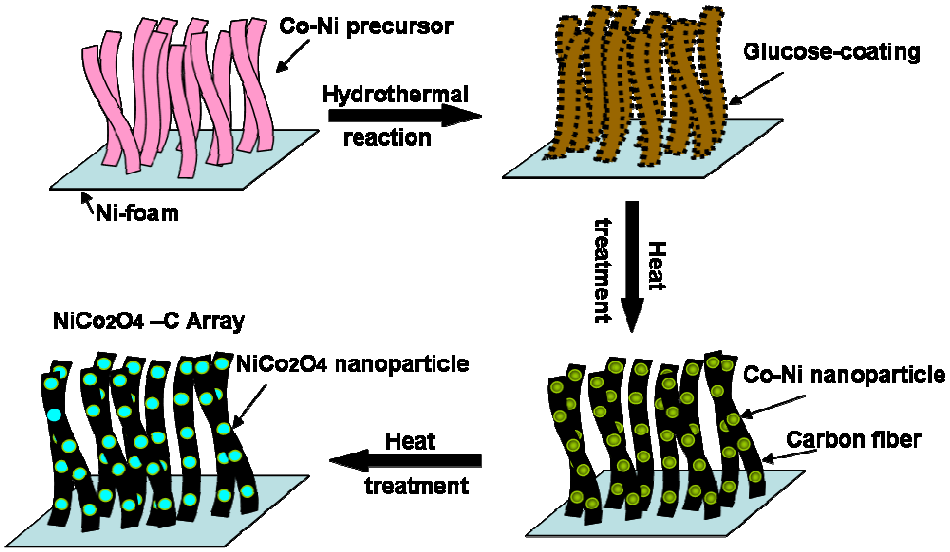

Fig. 1 Schematic illustration for the synthesis of the peapod-like $NiCo_2O_4$-C nanorods array on 3D Ni-foam is presented.

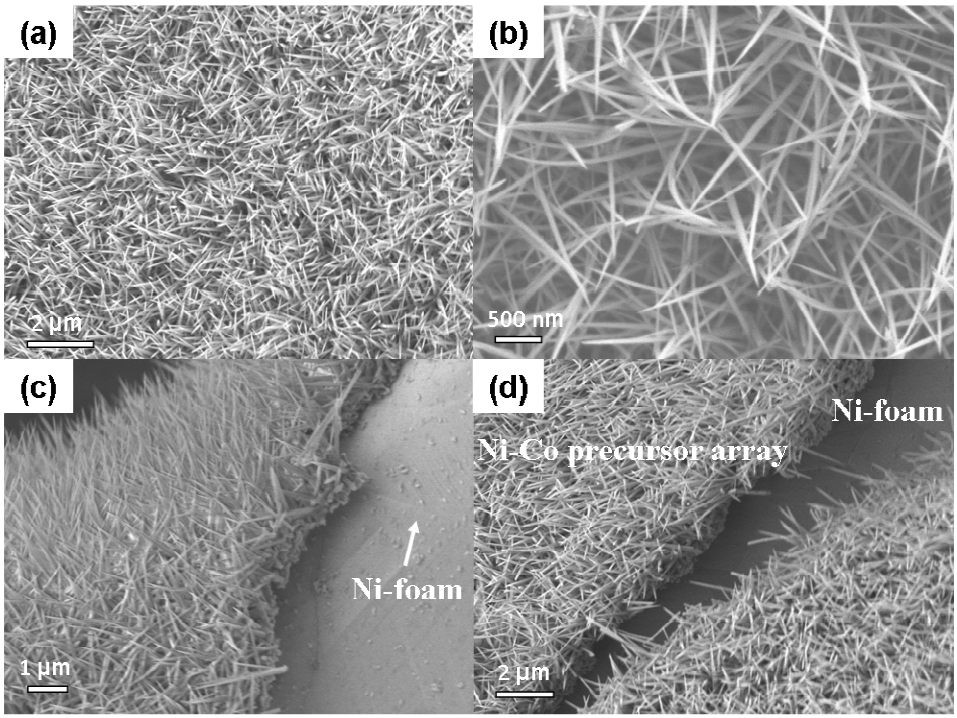

Fig. 2 (a) is the low-magnification SEM image via the top view to present the samples of Ni-Co precursor. (b) and (c) are the cross-section views to reveal the uniform 1-D nanorode structure of the Ni-Co precursor. (d) is the enlarged SEM image to disclose the regularly structure are aligned together.

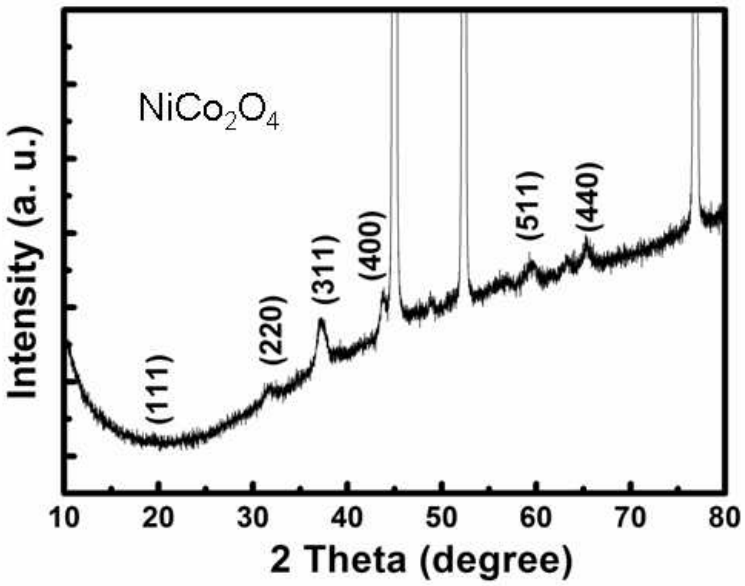

Fig. 3 XRD patterns to verify the obtained pure-phase $NiCo_2O_4$ on the Ni-foam (JCPDS 20-0781).

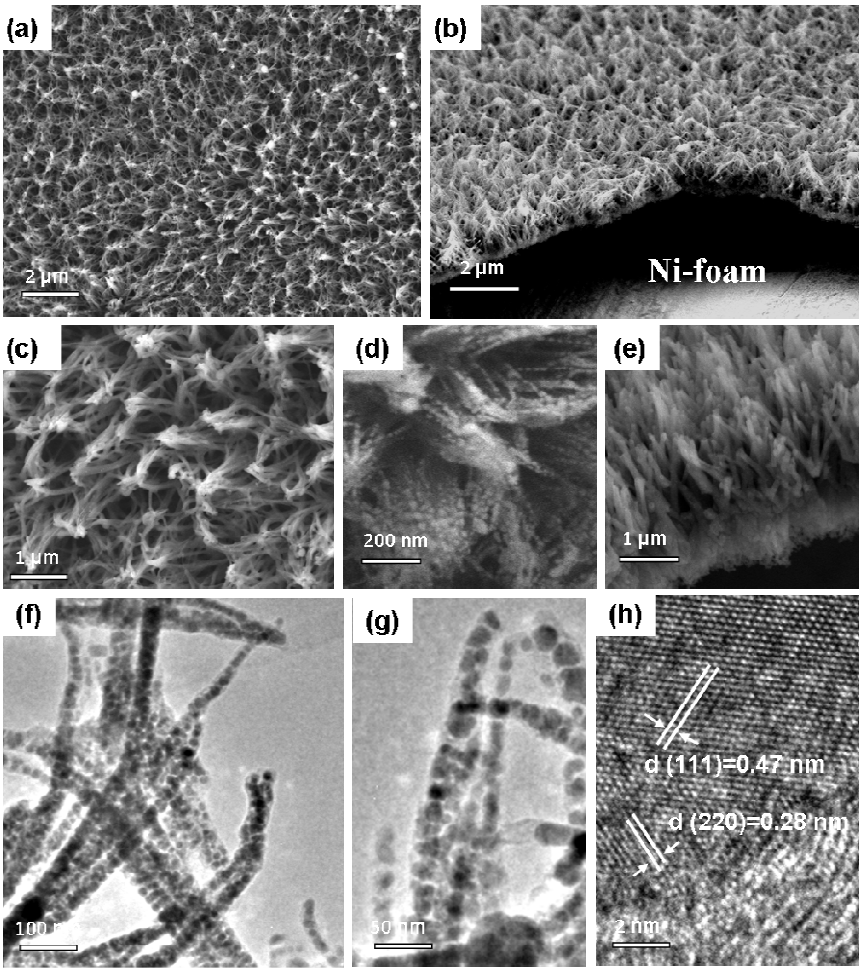

Fig. 4 (a) is a typical SEM image in while we can disclose that large scale production of the peapod-like NCO-C composite can be detected. (b) and (d) are the cross-section views of the peapod-like NCO-C composite. (c) is the low-magnification SEM image are introduced to show the unique peapod-like structure. (e) is the enlarged SEM image to reveal the specific structure. (f) and (g) are the typical TEM images to clearly present the peapod-like structure in which the $NiCo_2O_4$ nanoparticles uniformly embedded in the carbon shell. (h) is the HRTEM image to characterize the crystal structures of the embedded $NiCo_2O_4$ nanoparticles and graphitized carbon shell.

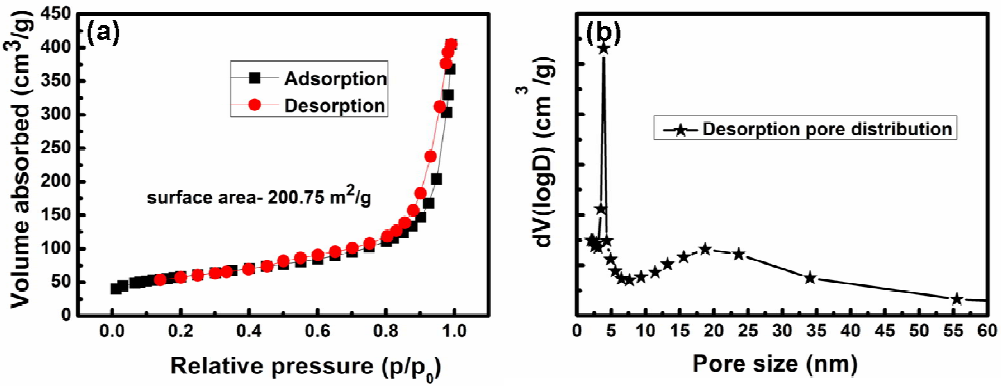

Fig. 5 (a) is the BET diagram proving high surface area for the peapod-like NCO-C composite. (b) is the corresponding pore size distribution.

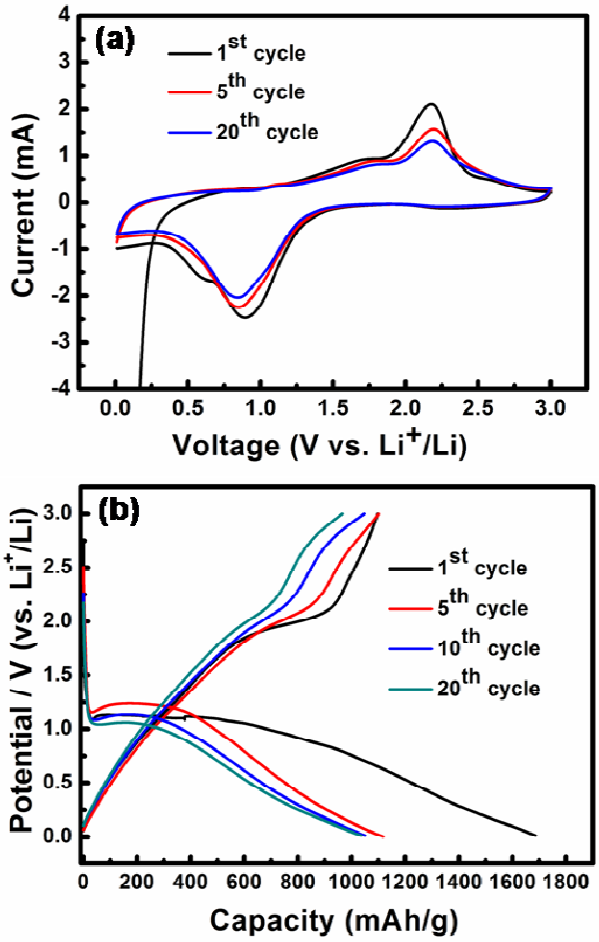

Fig. 6 (a) is the cyclic voltammetry (CV) profiles for the peapod-like NCO-C composite, proving the thermodynamic stability. (b) is the galvanostatic measurement curve at a current density of 100 mA g^{-1}.

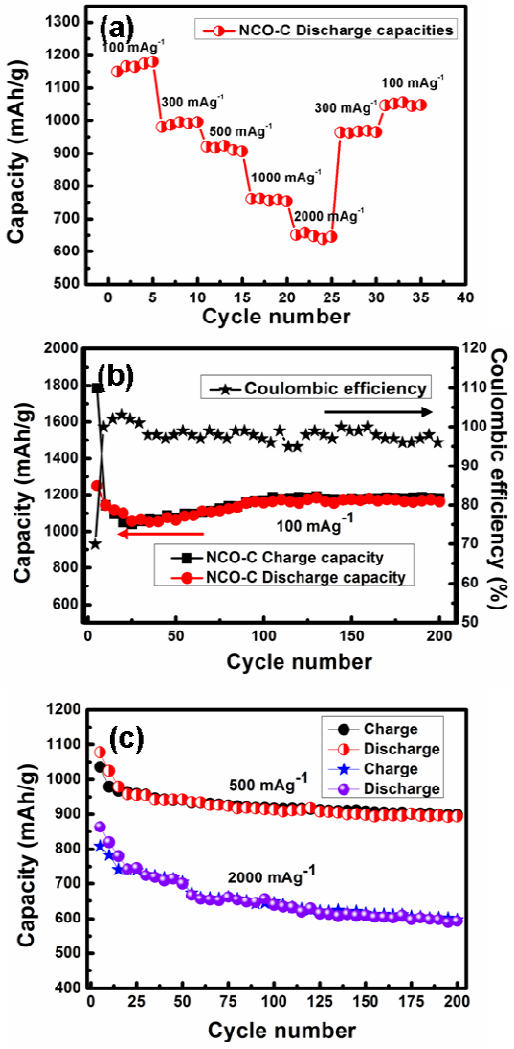

Fig. 7 (a) is the rate capability test on the peapod-like NCO-C nanorods array on the Ni-foam and (b) is the corresponding coulombic efficiency. (c) is the cycling performances of the peapod-like array at the current densities of 500 and 2000 mA g^{-1}.

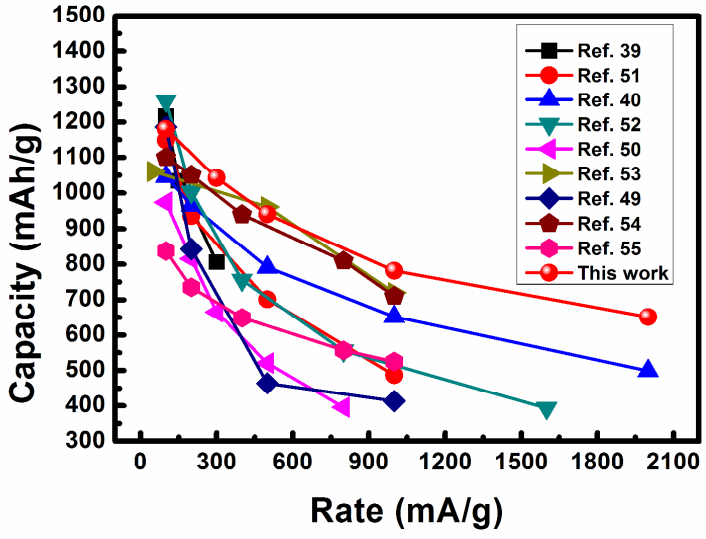

Fig. 8 Comparison of rate capability of peapod-like NCO-C nanorods array with other $NiCo_2O_4$-based anode materials reported recently.